Thin-Film Catheter-based Receivers for Internal MRI

R.R.A.Syms*, E. Kardoulaki, I.R. Young

EEE Dept., Imperial College London, Exhibition Road, London SW7 2AZ, UK

*TEL +44-207-594-6203 FAX +44-207-594-6308 Email r.syms@imperial.ac.uk

Ch. 9 in Micro and Nanoscale NMR Technologies and Systems,

Anders J., Korvink J. et al. Eds, Wiley-VCH (2018)

Introduction

Magnetic resonance imaging (MRI) is one of the major imaging modalities of medical diagnostics, offering an excellent combination of soft tissue contrast and resolution [1]. However, image quality is inherently limited by signal-to-noise ratio (SNR) [2] and often additionally by patient motion, especially in the abdomen [3]. The first consideration restricts the resolution, while the second introduces artefacts and prevents the improvement in SNR that can be normally obtained by signal averaging. The aim of this article is to describe developments to catheter-based radio-frequency (RF) receivers that might provide direct improvements in SNR when imaging internal structures. The devices are constructed using new thin-film technologies and have so far undergone no clinical evaluation, but nonetheless appear to offer a promising route to low-cost fabrication of high performance internal receivers.

Catheter receivers

The dominant noise sources in MRI are thermal, and arise from losses in the RF coil used for signal detection and in the body itself [2]. Both sources have uniform power spectra. Assuming normal room temperature, their absolute and relative magnitudes depend on many factors, including the Larmor frequency, the resistance, dimensions and field-of-view (FOV) of the coil, and the conductivity of the body tissue. Although conductor resistance rises with frequency due to the skin effect, body noise usually outweighs coil noise in human imaging. Unfortunately, noise cannot be localised using field gradients, and coils are sensitive to body noise from their entire FOV. SNR must therefore decrease as the voxel size is reduced, setting a limit to the useful

image resolution. To maximise the SNR, different receivers are used for different anatomical locations, matching the FOV to the target tissue [4]. Examples of external receivers include head, chest and spine coils. In many cases, the receiver is an array, which allows a larger image to be built up from signals from a set of local coils that individually have a smaller FOV for noise [5].

Internal imaging

Many internal coils have been developed on similar principles [6], for imaging large lumens such as the vagina, anus and gastrointestinal wall [7-9], and small lumens such as arteries [10-15]. To allow easier introduction, the coils are often mounted on an existing clinical tool. Large coils have been built into non-magnetic endoscopes [16-18] while smaller coils have been attached to catheters, either for imaging or for tracking [19-21]. Here we focus on catheter-based receivers, for which patient safety, clinical utility and small size all impose special difficulties.

To begin with, the catheter must be smooth and flexible, and capable of safe delivery into the relevant lumen. For arterial imaging, it may be inserted through an incision. To reach deep tissue, it may be inserted percutaneously or through a drainage tube [22]. However, non-surgical imaging of a new location such as the biliary ductal system will require a modification to endoscopic retrograde cholangiopancreatography [23], a procedure for biliary imaging that involves a side-opening duodenoscope and guidewire-compatible catheters. To justify an invasive procedure the catheter receiver must provide a resolution significantly exceeding that achievable using an external coil. However, imaging must be carried out without any RF-induced heating effects, which may arise from direct coupling to the magnetic field (B_1) or the electric field (E) of the transmitter during the excitation phase of MRI. Finally, all the electrical parts must be constructed cheaply and reliably in a circuit with a low form factor that may be easily mounted on a tubular scaffold. Catheter diameters are specified on the French (Fr) scale, with 1 Fr = 1/3 mm, and diameters typically range from 3-10 Fr, making the problem particularly challenging.

Catheter receiver designs

Many catheter receivers have already been demonstrated [24-25]. In each case, sensitivity

reduces with radial distance r from the axis. For a small, circular loop, sensitivity falls off as $1/r^3$, yielding a very small FOV [26]. In contrast, for the so-called 'loopless catheter antenna' [27] formed by extending the inner conductor of a coaxial cable a quarter of a wavelength beyond the sheath the sensitivity falls off as 1/r, greatly increasing the FOV. Unfortunately the loopless antenna suffers from an additional axial sensitivity variation. However its performance may be improved by insulation, tapering the whip, or forming it into a helical winding [28-29]. Other designs include solenoids [20], opposed solenoids [11, 12, 15, 21], elongated loops [9, 10, 13], and (for catheter visualisation) twisted pair cable [19]. Solenoids are constructed using a spiral of insulated wire, and opposed solenoids by reversing the direction of the winding at the midpoint. Elongated loops may easily be constructed from printed circuit boards (PCBs) or by short-circuiting a two-wire line [14]. Here they are of particular interest, because they are simple to construct using thin film circuits. Figure 1a shows a representative layout, with the long conductors parallel to the catheter axis. Such a coil is optimally sensitive to nuclear magnetic dipoles precessing about a static magnetic field $\underline{B}_0$ parallel to the coil axis, as shown in Figure 1b.

Elongated loop receivers

The reception pattern of any coil can be estimated from reciprocity [30], by considering the magnetic field $\underline{H}$ generated when unit current flows round the coil. For an elongated rectangular loop coil of width $s = 2x_0$ arranged parallel to the z-axis, two parallel cylindrical wires passing through the points $(\pm x_0, 0)$ can provide a reasonable approximation for calculation of the field [14]. In this case, $\underline{H}$ has components H_x and H_y, given by:

$$H_x = -(1/2\pi)\,[y / \{(x + x_0)^2 + y^2\} - y / \{(x - x_0)^2 + y^2\}]$$
$$H_y = (1/2\pi)\,[(x + x_0) / \{(x + x_0)^2 + y^2\} - (x - x_0) / \{(x - x_0)^2 + y^2\}] \qquad (1)$$

Figures 2a and 2b show contour maps of H_x and H_y respectively, with the inner clear region indicating a cylindrical catheter. Both patterns are highly non-uniform, and concentrate near the conductors. By reciprocity, the complex signal voltage V_S induced in the coil by a volume dv of dipoles precessing at angular frequency ω_L (the Larmor frequency) is $V_S = -j\omega_L \underline{B}_{xy} \,.\, \underline{M}_{xy}\, dv$. Here $\underline{M}_{xy}$ is the transverse magnetization, and $\underline{B}_{xy} = \mu_0(H_x \underline{u}_x + H_y \underline{u}_y)$, where μ_0 is the permeability of

free space and $\underline{u}_x$ and $\underline{u}_y$ are unit vectors in the x- and y-directions. Assuming B_0 also lies in the z-direction, $\underline{M}_{xy} = M(\underline{u}_x + j\underline{u}_y)$. For a 90° flip angle, the magnetization is entirely transverse, so $M = M_0$, where M_0 is the magnetization per unit volume. In this case, the peak voltage is:

$$|V_S| = \omega_L \mu_0 M_0 \sqrt{(H_x^2 + H_y^2)}\, dv \qquad (2)$$

Consequently, the quantity $\sqrt{(H_x^2 + H_y^2)}$ defines the signal reception pattern. Figure 2c shows the spatial variation of $\sqrt{(H_x^2 + H_y^2)}$, which loses all angular dependence at large radii. In fact, when $r >> x_0$, it is simple to show that $\sqrt{(H_x^2 + H_y^2)} = s/2\pi r^2$ [14]. Sensitivity is therefore proportional to the wire separation and falls off as $1/r^2$, a useful characteristic intermediate between the $1/r^3$ and $1/r$ variations previously mentioned. Even in this orientation, transverse images will still require correction for the $1/r^2$ sensitivity dependence. However, other coil orientations will have different reception patterns. For example, a coil set up with its axis and plane perpendicular to B_0 will be sensitive only to H_x, while a coil with its axis perpendicular and its plane parallel to B_0 will be sensitive only to H_y. The resulting non-uniformity is much less easily correctable, so imaging procedures must be carefully planned.

Tuning and matching

Additional circuitry is needed to achieve full functionality. To receive RF signals during the detection phase of MRI, the coil must be made resonant at the Larmor frequency. To transfer maximum signal power, its output impedance must be matched to the input impedance of the scanner's receiver electronics. To avoid heating and local over-excitation of the tissue, it must avoid coupling to the B_1 field, and be fitted with an output cable that minimises coupling to the E field. We now consider these additional requirements in some detail.

A coil with inductance L may be made resonant at f_L through the addition of a series capacitor C, such that $\omega_L = 2\pi f_L = 1/\sqrt{(LC)}$. Due to the limited conductivity of the windings, the coil inevitably has a series resistance R_C, and its performance as a tuned circuit is dictated by its quality factor $Q = \omega_L L/R$, with $R = R_C$. The magnetic field generated by precessing dipoles will induce a voltage V_S in the loop at the Larmor frequency by electromagnetic induction. However,

the signal source - a lossy dielectric - will transfer an additional resistance R_S into the loop, so that the total loop resistance will increase to $R = R_C + R_S$, reducing the Q-factor. One difficulty for small internal coils is that their Q-factors are inherently low. However, this effect may be offset by their small FOV, which renders them less sensitive to external loading.

There are several methods of matching the output of a resonant detector to a real load R_L. Generally these operate only over a narrow band. One example is capacitive matching, shown in Figure 3a. Here the capacitor C is separated into two components C_M and C_T in series. The load is connected across C_M (the matching capacitor), whose value is chosen to satisfy the impedance matching relation $\omega_L C_M = 1/\sqrt{(RR_L)}$. The value of C_T (the tuning capacitor) must then satisfy the series relationship $1/C = 1/C_M + 1/C_T$. Both values are normally determined by experiment, and several components must often be used to achieve suitable results. Depending on the parameters, matching can also be achieved using a shunt capacitor, or with a series or shunt inductor. Half-wavelength sections of coaxial transmission line may also be used to locate the matching components remotely from the coil [24], although this becomes increasingly difficult as ω_L rises, since the cable length must be proportionally shorter.

Alternatively, matching can be achieved by a mutual inductance, which allows the detection coil to be physically separated from the receive circuit. This approach is particularly useful for internal coils, since it allows signals to be transferred out of the body and into an external resonant circuit using purely magnetic coupling [31]. In this case, the equivalent circuit is as shown in Figure 3b. Here the external circuit is made resonant at ω_L using a capacitor C' and an inductor L' and coupled to the internal coil via a mutual inductance M. Near resonance, impedance matching is achieved when $\omega_L M = \sqrt{(RR_L)}$, and a suitable value of M can be achieved by adjusting the size, position and orientation of the external coil. However, this approach may be too time-consuming for a general investigative procedure.

B_1 field decoupling

Several solutions also exist to the problem of B_1 field decoupling. Figure 3c shows passive decoupling in a circuit with capacitive matching [32]. Here an inductor L_D is connected across C_T,

together with a pair of crossed diodes D. If induction gives rise to any significant current flow - as it might during excitation - the two diodes will conduct, effectively placing L_D in parallel with C_T and forming a tank filter. If L_D resonates with C_T at the Larmor frequency, the effect will be to insert a high resistance in the tuned circuit, significantly reducing the flow of current. However, if the induced current is low (as it is during detection) the diodes remain non-conducting, so L_D can be ignored and the main part of the circuit acts as a simple L-C resonator.

A similar principle is used in active decoupling [33], shown in Figure 3d. This time L_D is connected in series with the output, and a PIN diode P is placed across the output terminals. If P is held in reverse bias by the provision of a suitable DC voltage on the line (using additional circuitry, not shown), it will be substantially non-conducting. However, if P is placed in forward bias, it will conduct. In this case, L_D will be switched in parallel with C_M, again forming a tank filter that can block the flow of current in the resonant loop at the Larmor frequency. Most scanners provide suitable DC control signals, timed to operate at the start and end of excitation. The series reactance of L_D can easily be cancelled using an additional capacitor. However, if L_D is constructed using a length d of a coaxial transmission line (which will act as an inductor when short-circuited at one end), the output can simply be connected directly to the load using further coaxial cable as shown in Figure 3e. In this case, the characteristic impedance Z_0 of the cable should match R_L to prevent reflections throughout the system.

E-field decoupling

Any time-varying magnetic field (such as the B_1 field) must have an associated electric field. At low frequencies, this may largely be ignored, but at the frequencies associated with modern high field magnets its effects are significant. Particularly, the E-field may couple to the surface waves that can exist on extended conductors such as metal guidewires or the grounded shields of coaxial cables used for transmission of MRI signals out of the body. Such waves were originally investigated by Goubau [34], and have recently received attention because of their importance in MRI [35]. For cylindrical wires, a full field solution can be found by solving the electromagnetic wave equation in cylindrical co-ordinates. However, this is difficult for more complex geometries such as rectangular wires. Consequently, a qualitative description must suffice here.

The properties of the waves are strongly affected by the materials surrounding the conductor (typically a plastic insulating layer and the tissue itself). In the absence of an insulator, the electric field of the wave mainly exists in the tissue. As a result, its phase velocity is $v_{ph} \approx c/\sqrt{\varepsilon_r}$, where $c = 1/\sqrt{(\mu_0\varepsilon_0)}$ is the velocity of light, ε_0 is the permittivity of free space and ε_r is the relative permittivity of the tissue. Its wavelength is therefore $\lambda = v_{ph}/f_L$, and resonance can occur whenever the inserted length is a whole number of half wavelengths, as shown in Figure 4a. The shortest such length occurs when $d = v_{ph}/2f_L = c/(2f_L\sqrt{\varepsilon_r})$. At the frequency of a 1.5 T scanner, the dielectric constant of most tissue is high ($\varepsilon_r \approx 77$ [36]), and the critical length is $d = 3 \times 10^8/(2 \times 63.85 \times 10^6 \times \sqrt{77}) = 0.27$ m, a length comparable to typical insertion distances. The effect of the insulator is to reduce the effect of the tissue; however, only thin insulators are practical.

The consequence of resonance can be understood in terms of the equivalent circuit in Figure 4b [35]. Here, the conductor is modelled as the upper wire in a transmission line, with the lower ground wire modelling currents returned through the body. The circuit is divided into a many small sections. The magnetic properties of the surround are modelled as series inductors of value μ_0, and the dielectric properties as shunt capacitors of value $\varepsilon_0\varepsilon_r$. Excitation is modelled by voltage sources V_E, which cause a current I_n to flow in the n^{th} section. For sufficiently short sections, this model predicts the existence of travelling current and voltage waves with the correct velocity, namely $c/\sqrt{\varepsilon_r}$. At resonance, the currents I_n form a discrete approximation to the sinusoidal pattern in Figure 4a. Without loss, the peak current is infinite; however, insertion of resistors modelling losses in the tissue and wire allows it to remain finite. The corresponding nodal voltages V_n form a cosinusoidal pattern, with positive and negative maxima at either end of the line. These voltages cause large shunt currents to flow through the surrounding medium at each end, which in practice give rise to rapid and potentially dangerous tissue heating [37, 38].

Several strategies have been developed to reduce RF heating. The conductors may be subdivided, by inserting current-blocking impedances (inductors or resonant tank filters) at regular intervals a $< \lambda/2$ as shown in Figure 5a [39, 40], and the direction of the conductors may be periodically reversed [41]. Alternatively, both conductors of a two-wire circuit such as a transmission line

may be segmented, by inserting coupling transformers at regular intervals as shown in Figure 5b [42]. In this case, additional capacitors are required as tuning and matching networks, and the inductors forming the transformers must be formed into figure of-eight loops to avoid coupling to the B_1 field [43]. Finally a similar approach based on a magneto-inductive (MI) waveguide [44, 45] shown in Figure 5c may be used. In this case, the transmission lines and matching networks in Figure 5b are omitted, and matching is carried out by the mutual inductances M.

Thin-film catheter receivers

Conventionally, catheter receivers are constructed using manual assembly of wound coils with surface-mount device (SMD) capacitors and diodes. However, the resulting devices are bulky, fragile and lack repeatability. Here we describe how receivers can be constructed using industrial production methods. There are a number of difficulties. Everything must be achieved using non-magnetic materials, and all components must be smooth, flexible, and have a low form factor. Modern approaches are universally based on techniques previously investigated for miniature NMR systems, namely microfabrication of conductive tracks on dielectric substrates [46]. Two alternative techniques are used: patterning and etching of deposited copper, and electroplating of copper in a patterned mould. Originally, substrates were rigid [47, 48], but flexible substrates are increasingly used [49-51] and capacitors and inductors are now integrated together to simplify tuning and matching [52]. Non-linear components such as diodes, which cannot easily be integrated, are often omitted and alternative solutions to decoupling are found.

Thin film coils

We first note that planar processing introduces inherent topological limitations. Solenoids, which require a conductor to be wound round the catheter, are difficult to fabricate. Although specialised methods such as microcontact printing [53], laser lathe lithography [54] and wire bonding [55] have been developed for this purpose, these cannot easily form other parts of the circuit. The focus here is therefore on elongated loops, with long conductors parallel to the catheter axis and short conductors passing half way around the circumference. Inductors are normally restricted to one- or two-turn layouts, as the advantage of additional turns is quickly lost

in a small concentric spiral. However, all planar spirals require connections between the inner and outer turns. These can be made using an air-bridge passing or a conductive via through the substrate. For example, Figure 6a shows a two-turn spiral, with an air-bridge connection to landing pads for SMD matching and tuning capacitors C_M and C_T [56]. The structure can be formed entirely by single-sided processing. However, this approach provides no real integration, and requires two layers of patterning and plating to form the air-bridge.

Figure 6b shows an alternative approach based on patterning of conductors on both sides of the substrate [56]. Here C_M and C_T are formed as integrated parallel plate capacitors, using the dielectric as an interlayer. Only two patterning steps are required, and the connection between the inner and outer turns of the spiral is now made using backside metal. The capacitors may easily be trimmed using a scalpel, providing a simple method of tuning and matching. The last aspect is especially important, since the inductance generally alters when the circuit is mounted on a catheter. Coils of this type have been fitted with a sub-miniature coaxial output cable, which is passed through the central lumen of a hollow catheter scaffold. For short catheters, additional active decoupling has also been fitted, mounting the bulky PIN diode outside the catheter. However, further integration is required for more general clinical use.

Thin-film interconnects

Provision of a thin-film transmission line on the outside of the catheter will avoid blocking its central lumen. In principle, several suitable structures exist. For example, Figure 7a shows microstrip [57], which consists of a single conductor separated from a ground plane by a dielectric interlayer. Similarly, Figure 7b shows symmetric coplanar waveguide (CPW) [58], which has ground planes on either side of the conductor, all in a single layer of metal. In each case, the characteristic impedance is $Z_0 = \sqrt{(L_p/C_p)}$, where L_p and C_p are the per-unit length inductance and capacitance between the signal wire and ground, respectively. Both designs have drawbacks. If the dielectric is thin and the conductor is wide, microstrip will have a high value of C_p and a low value of L_p, and consequently a low value of Z_0. Similarly, if the gaps between conductors are large, CPW will have a low value of C_p, a high value of L_p and a low value of Z_0. In each case, it is difficult to achieve 50 Ω impedance, a standard value simplifying matching.

A solution is provided by the structure in Figure 7c, which contains a signal conductor on one side of the substrate and a periodically patterned ground on the other [59], and effectively consists of alternating sections of microstrip and CPW. At low frequencies, it therefore operates as a waveguide with intermediate impedance. However propagation cuts off at high frequency and the structure belongs to the class of electromagnetic bandgap (EBG) devices. The cut-off frequency and impedance are both controllable (the former by adjusting the period, and the latter by the relative size of the holes in the ground plane) [60]. EBG cables have been combined with resonant detectors to form complete receivers as shown in Figure 7d [61]. In principle, a PIN diode may also be added at a suitable point along the output cable to allow active B_1 field decoupling. However, the structure cannot be considered MR-safe, due to the possibility of exciting surface waves. To avoid this problem, a more radical redesign is required.

MR-Safe thin film interconnects

Several design changes are required to increase inherent safety, as previously discussed with reference to Figures 4 and 5. Magnetic excitation of resonances can largely be avoided by adopting a symmetric figure-of-eight layout for any resonant element. Voltages induced in either half of the element by uniform B_1 fields will cancel, reducing the need for non-linear components to provide further protection. However, the circuit will still be sensitive to MRI signals during detection, since these fields are not uniform. Although a figure-of-eight must involve crossing conductors, a suitable layout may be provided as shown in Figure 8a. Here the two halves each have inductance L/2, and the loop is completed and made resonant with two capacitors, each of value 2C. Electrical excitation of resonances can largely be prevented, by segmenting the circuit into lengths shorter than a half wavelength. One approach is the MI waveguide in Figure 5c. Such circuits have received extensive attention from metamaterial scientists, and the application to MRI has been pointed out [62].

Analysis of a MI waveguide is relatively simple. In an infinite system, the current I_n in the n^{th} element can be related to the currents in neighbouring elements by the recurrence relation [44]:

$$(R + j\omega L + 1/j\omega C)I_n + j\omega M(I_{n-1} + I_{n+1}) = 0$$

(3)

Assumption of a solution in the form of a travelling current wave, as $I_n = I_0 \exp(-jka)$, where I_0 is the wave amplitude, k is the propagation constant and a is the period, leads to the following relation between the propagation constant and frequency [45]:

$$(1 - \omega_0^2/\omega^2 + j/Q) + \kappa \cos(ka) = 0$$

(4)

Here $\omega_0 = 1/\sqrt{(LC)}$ is the angular resonant frequency of the elements, $Q = Q_0\omega/\omega_0$, where $Q_0 = \omega_0 L/R$ is the Q-factor, and $\kappa = 2M/L$ is the coupling coefficient (which may be positive or negative, depending on the physical arrangement and the sign of the mutual inductance M).

The presence of losses in the form of the resistors R will render the propagation constant complex, as $k = k' - jk''$. Substitution into the dispersion equation, equating real and imaginary parts to zero and assuming that losses are small yields the two separate equations:

$$(1 - \omega_0^2/\omega^2) + \kappa \cos(k'a) \approx 0$$
$$k''a \approx 1/\{\kappa Q \sin(k'a)$$

(5)

The first is the lossless dispersion equation. It is simple to show that propagation is allowed only over the finite frequency band $1/\sqrt{(1 + |\kappa|)} \leq \omega/\omega_0 \leq 1/\sqrt{(1 - |\kappa|)}$. The effect of a finite Q-factor is to allow out-of-band signals and introduce propagation losses. Loss is minimised at resonance, when $k'a = \pi/2$. However, low losses require large coupling coefficients and high Q-factors. Unfortunately, both are limited, especially for small resonators. As a result, propagation losses are normally higher than in conventional transmission lines, a clear trade-off for increasing safety.

MI waveguides have been demonstrated using conventional inductors and capacitors [45], and also using printed thin films [63]. Thin film cables are largely immune to the effects of bending [64] and have moderate noise figures [65]. For MRI signal transmission, a suitable arrangement

can be constructed by overlaying figure-of-eight resonators as shown in Figure 8b [66]. Here, consecutive inductors are printed on opposite sides of the substrate, and overlaid so that approximately half of each element overlaps its neighbour on either side. The overall element length must clearly be below the critical length d previously discussed. However, in this arrangement the period a can approach d/2 and the number of elements is minimised. The coupling coefficient κ is positive and limited to a maximum value of unity; in practise, values above 0.65 are routinely obtained. A resonant detector can be formed as a similar element, merely differentiated by an adjustment in its overlap with its neighbour as described below. Clearly, all the resonant elements are sensitive to external RF signals, and consequently the structure should be capable of forming an MRI image along its entire length, albeit with image intensity variations where the conductors cross each other [66].

Matching at either end of the line can be carried out as follows. The characteristic impedance of a MI waveguide is $j\omega M \exp(-jka)$, which reduces to the real value $Z_{0M} = \omega_0 M$ at resonance [44]. Impedances close to 50 Ω have been obtained in thin film systems; however Z_{0M} is normally somewhat lower due to limitations on the mutual inductance. Matching to the scanner electronics can be achieved using the inductive method previously described. All that is required is to connect the MI waveguide to R_L via a further resonant element with a mutual inductance M' that satisfies the impedance matching relation $\omega_L M' = \sqrt{(Z_{0M} R_L)}$. This can be done using a removable resonant coupling tap, whose position can easily be adjusted. Matching to the detector itself can be achieved in the same way, by adjusting the overlap b between the detector and the MI waveguide so that the mutual inductance satisfies the similar relation $\omega_L M'' = \sqrt{(Z_{0M} R)}$. However, once this has been done, the detector must be fixed in place.

Thin-film device fabrication

Small thin-film devices can be fabricated using modified semiconductor processing, by attaching thin-film substrates to silicon carrier wafers. However, significant advances followed from the adoption of the industrial roller processes used for flexible printed circuit board manufacture, which can yield circuits in the lengths of several metres required for complete catheter probes.

Design and modelling

Design layouts can be achieved by iteration. Component lengths, widths and areas are first estimated, together with CAD layouts that allow the components to fit within the outside dimensions of the catheter scaffold. The simple parallel plate formula can be used to estimate capacitor values, while the freeware software package FastHenry (MIT, Cambridge, MA) provides a convenient method of estimating inductor values. A three-dimensional electromagnetic simulation of the resulting circuit is a lengthy procedure. However, useful simulations can be carried out using quasi 3D solvers. For example, the commercial software Microwave Office® (AWR Corp., El Segundo, CA) allows multi-layered 2D circuits to be modelled within a stacked layer of materials. This geometry is flexible enough to allow investigation of different substrates, insulators and tissue-type surrounds, and simulation of tuning and matching, detection, and coupling to external electric and magnetic fields. Detailed simulations of MI catheter receivers have been carried out, which confirm the inherent lack of sensitivity to external B_1 and E fields [67].

Once a design has been established, its parameters can be fine-tuned following fabrication and testing. Frequency scaling to operate at higher magnetic fields is also relatively simple. The resonant frequency of an L-C resonator is $\omega_L = 1/\sqrt{(LC)}$. Since the inductance L and capacitance C of long, thin components are approximately proportional to their length, operation of a design at double the frequency can be achieved by halving the length of a resonant element. Conveniently, this geometric scaling also applies to the critical length for standing wave resonances, so that nominally MR-safe characteristics are retained during scaling [68].

Materials and fabrication

The most suitable thin-film dielectric material is polyimide, a pinhole-free substrate that is manufactured commercially by E.I. Dupont de Nemours and Co. (Circleville, OH, USA), under the trade name Kapton® HN [69]. Standard thickness values are 6, 13, 25, and 50 μm; however, 25 μm thick films provide the optimum combination of mechanical and electrical properties. A

larger thickness increases the surface area of the capacitors (which may then be too large to arrange on the circuit) and consequently the mechanical stiffness. However, thinner substrates can be prone to wrinkles during processing. Thick copper conductors may be fabricated by electroplating inside a mould. However, additional sputtered metal layers are required for adhesion, care is required to achieve low-stress layers, and the final conductivity is relatively low [56]. Improved performance is obtained by patterning and etching 35 μm thick layers of pressure-bonded copper, whose conductivity is close to that of bulk material.

Thin-film PCBs are fabricated as shown in Figure 9a [60]. Patterning is carried out by photolithography and wet chemical etching. Small circuits are patterned in a single exposure, but complete catheter circuits require stepped exposure. Photomasks are formed from Mylar-coated silver halide on polyester in lengths up to 1 metre, and the PCB is sensitised with a 175 μm thick layer of laminated photoresist (1). The sensitised PCB is then sandwiched between two masks on a glass backing, using mechanical pins to align the front and rear patterns. Each side is exposed with an UV lamp, and the process is repeated in a second exposure (2). The resist is then developed and the pattern transferred to the copper beneath by etching. Finally, the resist is stripped. Circuits have been fabricated by Clarydon (Willenhall, West Midlands, UK) in arrays of 24, with a line width and separation of 0.5 mm and excellent front-to-back alignment.

Catheter receivers are constructed by separating individual circuits from the panel and attaching them to the outside of tubular scaffolds (which are supported on a length of wire during assembly) using heat-shrink tubing as shown in Figure 9b. A scaffold diameter of 2.2 mm yields an outside diameter of ≈ 3 mm, small enough to pass the biopsy channel of an endoscope. Adjustment of capacitor values can be carried out with the circuit loosely attached with tape. For conventional receivers, connections can be made using sub-miniature coaxial cable, while demountable resonant inductive transducers can be used for magneto-inductive systems.

Figure 10 shows typical thin-film components. Figure 10a shows a resonant detector based on a 60 mm long two-turn spiral inductor with integrated tuning and matching capacitors [70, 71]. Active decoupling has been fitted to such components using non-magnetic PIN diodes (MA4P7464F-1072, M/A-COM Technology Solutions, Lowell, MA, USA) and lengths of sub-

miniature non-magnetic co-axial cable (0.8 mm diameter 50 Ω Bluetooth cable, Axon Cable, Dunfermline, UK). Figure 10b shows an EBG waveguide with a period of 16 mm and a mark-to-space ratio b/a = 1/8 in the ground-plane pattern, and Figure 10c shows the cable section of a receiver formed by combining a spiral resonator with an EBG waveguide, after mounting on a catheter [61]. Figure 10d shows the final section of a MI waveguide receiver with an element length of 200 mm, and Figure 10e shows the cable section of the assembled MI catheter receiver. Finally, Figures 10f and 10g show a resonant transducer, before and after mounting in a split clamp to allow attachment to a catheter receiver [72].

Mechanical performance

Using a tubular scaffold, the receivers are intrinsically compatible with a guidewire, as shown in Figure 11a. However, all catheters must have low stiffness to accommodate normal anatomy or the internal layout of an instrument. They must also have low friction and be 'pushable', to avoid buckling during insertion [73]. These requirements introduce additional constraints on materials and design. For example, layouts such as the spiral resonator in Figure 6b that include short, wide capacitors contain large metallic areas. These introduce regions of high stiffness, rendering the resulting catheters suitable only for semi-rigid applications such as MRI temperature monitors attached to laser thermal ablation probes [70]. However, the Kapton substrate has moderate transparency to near infrared radiation from a Nd: YAG laser, a key optical requirement for this application [71]. EBG cables, which have continuous ground planes, have similar mechanical characteristics. However, MI waveguides contain only narrow, elongated metallic regions, and consequently have intrinsically low stiffness. Using an elastomeric heat-shrink to ensure low friction, MI catheter receivers can incorporate a soft tip and be flexible enough to pass the biopsy channel of a non-magnetic side-opening duodenoscope [74] as shown in Figure 11b.

In addition, receivers must not detune significantly when bent. Since the properties of long, thin inductors are relatively immune to mechanical deformations that do not alter conductor spacing [64], none of the receiver systems described appear sensitive to bending. For example, MI catheter receivers have an elongated element layout that has already been shown to bend through a radius of 5 mm without detuning [72].

Electrical performance

Electrical performance can be measured using an electronic network analyser (ENA). Here, measurements were carried out using an Agilent E5061A instrument. Actual component values are first recovered from experiments on simpler circuits, and used to correct design layouts. For example, an inductor value may be determined by removing the integrated capacitor from a resonant element, making the circuit resonant again using a known capacitor, and measuring the resonance using inductive probes. Once the inductance is known, the integrated capacitance can be found from the original resonance, while the internal resistance may be found from the Q-factor. Similarly, the coupling coefficient κ in a MI waveguide may be found by measuring the frequency split of the two resonances obtained from a pair of coupled elements. Once κ is known, the characteristic impedance of the guide can be estimated, and the matching conditions established. Despite this, variations in component values do still arise. Lithographic alignment errors alter capacitor values, while mounting on a cylindrical scaffold alters inductor values. However, in each case, the capacitors can be trimmed before assembly to compensate.

Once component layouts are established the circuits can be adjusted very simply. To optimise a spiral resonator, the output is connected to the ENA using conventional cable. The frequency variation of reflection (S_{11}) is monitored as C_T and C_M are trimmed, with the position and depth of the minimum in reflection indicating the resonant frequency and degree of matching. For example, Figure 12a shows successive variations in S_{11} obtained as a 60 mm long spiral resonator is tuned for 1.5 T operation. Here, the resonant frequency is initially too low and the matching poor (1); however, after adjustment, the resonance is correctly established and the matching is corrected (2). Transmission through the circuit (S_{21}) is then measured using an additional inductive probe, showing that the detector has a Q-factor of ≈ 20 (Figure 12b). Although tuning is fixed, the resonant frequency can be tuned slightly too high, to compensate for loading effects [61]. Improved performance is obtained by operating at higher frequencies, although the advantage expected from frequency scaling is reduced somewhat by the skin effect. Figure 13a shows the frequency response after tuning for 3.0 T operation; here the Q-factor has risen to ≈ 30.

Active decoupling based on the circuit in Figure 3e may be assessed in a similar way. The control signal for the PIN diode can be derived from a signal generator, and connected between the S_{11} port and the detector using a passive splitter. Figure 13b shows the frequency variation of S_{21} for an actively decoupled resonator. Two states are shown. In the receive state (RX) the PIN diode is reverse-biased, and the detector has a normal resonant response. In the transmit state (TX), the diode is forward biased. The effect is to convert the circuit into a system with two resonant peaks, which may be placed on either side of the Larmor frequency adjusting the length d of the coaxial inductor. In this case, the response in the TX state is ≈ 35 dB below that in the RX state, a useful reduction in sensitivity that will provide effective decoupling from B_1 fields.

To assess an EBG cable, it is simply connected between the S_{11} and S_{21} ports and the frequency variations in reflection and transmission are measured. To optimise the design, layouts with different mark-to-space ratio b/a can be assessed, and the value giving minimum reflection identified. Figure 14a shows the frequency variations in S_{11} and S_{21} obtained for a two metre-long cable, which shows low reflection and low loss at low frequency and a high-frequency cutoff at 2.5 GHz, well above MRI frequencies [69]. Figure 14b shows the response of a complete receiver, formed by combining a resonant detector with an EBG cable [60]. Performance is clearly similar to that of a conventional resonator, confirming the viability of thin-film solutions.

To assess a MI waveguide, it is also connected between the S_{11} and S_{21} ports, this time using demountable resonant transducers. The frequency variations in reflection and transmission are measured, while adjusting the transducer positions to optimise the matching at either end. Figure 15a shows the frequency variation in S_{11} and S_{21} obtained for a two metre-long cable, which clearly demonstrates the band-pass nature of the transmission characteristic [72]. Reasonable impedance matching has been achieved, and minimum attenuation is around 3.8 dB/m. Figure 15b shows the response of a complete receiver, after matching has been optimised by adjusting the position of the final element as shown in Figure 8b. Despite the unusual nature of the magneto-inductive interconnect, resonant behaviour can again be clearly seen.

Magnetic resonance imaging

Thin film detectors have been evaluated in several clinical scanners, operating at 1.5 T (GE Signa Excite) and 3.0T (GE Discovery MR 750 and Philips Achieva). Connection was made via an auxiliary coil port, in the last case using a custom interface (Lambda Z Technologies, Baltimore, MD). Conventional receivers operated without alteration; however, MI receivers required the addition of a non-magnetic PIN diode across the input connections to pass coil pre-scan tests.

Imaging with resonant detectors

The emphasis to date has been on demonstrating functionality and comparing achievable SNR in phantoms and excised tissue specimens against the performance of standard external coils such as cardiac arrays. Phantoms have contained either a water-based tissue-simulating solution (3.268 g/l $NiCl_2.H_2O$, 2.4 g/l NaCl, conductivity $\sigma \approx 0.3$ S/m, relative permittivity $\varepsilon_r \approx 77$) or, to prevent convection in heating experiments, an agar gel with similar doping. For example, Figure 16a shows a typical experiment carried out using a catheter-mounted resonant spiral microcoil [70]. Here the coil has been embedded axially in a moulded cylindrical gel phantom, which is in turn surrounded by additional gel. Further loading for an 8-element cardiac array coil (not shown) is provided using two standard cuboid phantoms. Excitation was carried out using the system body coil. Imaging was carried out using a spin echo sequence, and comparative images were obtained using the array and the microcoil. Figure 16b shows an axial slice across the phantom obtained using the array coil, which has very uniform sensitivity. Here the cylindrical phantom may be clearly seen, together with surrounding rectangular blocks used for loading. Limited over-excitation can be seen in the vicinity of the central microcoil, implying reasonable decoupling.

Figure 17a shows the corresponding raw image obtained from the microcoil, which at first sight has an extremely restricted FOV. However, Figure 17b shows the same image after correction for the $1/r^2$ sensitivity variation. The detail in Figure 16b is now apparent, albeit with a SNR that deteriorates with r. Numerical values of SNR can be extracted from such images by standard methods, and Figure 17c shows the variation of SNR in a horizontal line through the microcoil. The array provides a uniform SNR, albeit limited to around 100. In contrast, the microcoil provides a non-uniform SNR, decreasing with radial distance. However, near the catheter, the SNR is much higher, and peak values close to 1200 are obtained on either side. Thus, the

microcoil offers a clear SNR advantage over a limited FOV. In this case, a four-fold advantage is obtained up to a diameter of ≈ 20 mm, over six times the catheter diameter. This improvement is extremely significant, since it can only be obtained by averaging signals for sixteen times as long.

Imaging with EBG detectors

Imaging has also been carried out with an EBG catheter receiver [61]. In this case, the receiver was tuned for 1.5 T operation, but active decoupling was omitted for simplicity. Excitation was carried out using the system body coil and reception using the EBG receiver, using a 3D GRE (gradient echo) sequence. Multiple excitations were required to improve SNR, and the imaging time was lengthy (almost 8 minutes). Despite these limitations, this experiment represents the first example of image transfer along a thin-film output cable. Figure 18a shows the subject for imaging, an ex vivo pig's liver, with the EBG catheter inserted into an accessible bile duct. Figure 18b shows an axial slice image. Due to the lack of decoupling, there is some local over-excitation. Despite this, useful anatomical detail including adjacent ducts can be seen. The small voxel size suggests sub-millimetre resolution and implies the future possibility of detecting tumours that cause variations in thickness of a bile duct wall, or breaching of the duct wall integrity with infiltration into surrounding tissue.

Imaging with MI detectors

Because of the inherent safety advantages, subsequent experiments have been carried out exclusively with magneto-inductive catheter receivers. For example, Figure 19a shows a phantom imaging experiment, involving a 2 m long MI catheter arranged in a spiral racetrack on top of a cuboid phantom [66]. Figure 19b shows a coronal image obtained at 1.5 T, from the tissue simulating fluid immediately beneath the catheter. Clearly, an image is obtained along the entire length of the catheter, which has not been detuned by the curved track. The images are obtained in segments, with each segment corresponding to one half of the figure-of-eight elements used. The image is brightest at the sensitive catheter tip, a characteristic that combines sensitive distal imaging with inherent catheter visibility. Figure 20a shows a later phantom experiment, emulating the MR imaging of a cannulated bile duct [72]. Here a magneto-inductive catheter has

been passed through the biopsy channel of a plastic model of a duodenoscope tip, and is emerging from the side port after being bent through around 90° by a remotely actuated tip deflector. The entire arrangement is immersed in tissue-simulating fluid, and Figure 20b shows a sagittal image obtained using a spin-echo sequence. Despite the bending of the catheter, a bright image is obtained at the catheter tip, and even details internal to the model duodenoscope such as the catheter deflector can be seen. Further work has been carried out to compare the SNR achievable from that obtained using external coils. Local advances of the type shown in Figure 17b have been obtained [75], despite the moderate noise figure of the MI cable [65].

Such experiments suggest encouraging imaging performance. However, extensive safety testing is required before in vivo experiments can be carried out. These have been partially completed. The use of a figure-of-eight element shape has been shown to convey reasonable immunity to B_1 fields, even for bent elements, and lengthy exposure to RF-intensive sequences has so far failed to give rise to any significant heating from elements fully immersed in gel phantoms [67, 72].

Conclusions

Thin film technology appears to offer many new solutions to the problem of constructing catheter receivers for internal MRI. Industrial manufacturing methods have successfully adapted to form thin-film circuits for signal detection and safe signal transmission that may be easily integrated on a hollow catheter scaffold. Although the technology is relatively complex to develop, the manufacturing method leads to systems that are smooth, flexible, and guidewire compatible. They are also highly repeatable, and largely avoid the lengthy tuning and matching process needed in equivalent manually assembled systems. Further work is clearly required to confirm intrinsic safety in vivo, demonstrate clinical utility, and verify that the local SNR advantage can be maintained in vivo, despite patient motion. In addition, although the receivers are generally robust, further work is required to improve general mechanical and electrical reliability. This work is ongoing.

Acknowledgements

The Authors gratefully acknowledge the sustained contribution of their collaborators Prof. Simon Taylor-Robinson, Prof. Wady Gedroyc, Dr Chris Wadsworth, Dr Marc Rea, Prof. Laszlo Solymar, Dr Munir Ahmad and Dr Mike Ristic to this work.

References

1. McRobbie, D.W., Moore, E.A., Graves, M.J. and Prince, M.R. (2006*) MRI from proton to picture* Cambridge University Press, Cambridge.
2. Hoult, D.I. and Lauterbur, P.C. (1979) The sensitivity of the zeugmatographic experiment involving human samples. *Journal of Magnetic Resonance*, 34(2), 425-433.
3. Schultz, C.L., Alfidi, R.J., Nelson, A.D., Kopiwoda, S.Y. and Clampitt, M.E. (1984) The effect of motion on two-dimensional Fourier transformation magnetic resonance images. *Radiology*, 152(1), 117-121.
4. Kneeland, J.B. and Hyde, J.S. (1989) High-resolution MR-imaging with local coils. *Radiology*, 171(1),1-7.
5. Roemer, P.B., Edelstein, W.A., Hayes, C.E. et al. (1990) The NMR phased array. *Magnetic Resonance in Medicine*, 16(2), 192-225.
6. Gilderdale, D.J., deSouza, N.M., Coutts G.A., et al. (1999) Design and use of internal receiver coils for magnetic resonance imaging. *British Journal of Radiolology*, 72(864), 1141-1151.
7. Baudouin, C.J., Soutter, W.P., Gilderdale, G. and Coutts, G.A. (1992) Magnetic resonance imaging of the uterine cervix using an intravaginal coil. *Magnetic Resonance in Medicine*, 24(1), 196-203.
8. De Souza, N.M., Kmiot, W.A., Puni, R., et al. (1995) High resolution magnetic resonance imaging of the anal sphincter using an internal coil. *Gut*, 37(2), 284-287.
9. Armenean, M., Beuf, O., Pilleul, F. and Saint-Jalmes, H. (2004) Optimization of endoluminal loop radiofrequency coils for gastrointestinal wall MR imaging. *IEEE Sensors Journal*, 4(1), 57-64.
10. Kantor, H.L., Briggs, R.W. and Balaban R.S. (1984) In vivo ^{31}P nuclear magnetic resonance measurements in canine heart using a catheter-coil. *Circulation Research*, 55(2), 261-266.

11. Martin, P.J., Plewes, D.B. and Henkelman, R.M. (1992) MR imaging of blood vessels with an intravascular coil. *Journal of Magnetic Resonance Imaging*, 2(4), 421-429.
12. Hurst, G.C., Hua, J., Duerk, J.L. and Cohen A.M. (1992) Intravascular (catheter) NMR receiver probe: preliminary design analysis and application to canine iliofemoral imaging. *Magnetic Resonance in Medicine*, 24(2), 343-357.
13. Kandarpa, K., Jakab, P., Patz, S., Schoen, F.J. and Jolesz F.A. (1993) Prototype miniature endoluminal MR imaging catheter. *Journal of Vascular and Interventional Radiology*, 4(3), 419-427.
14. Atalar, E., Bottomley, P.A., Ocali O. et al. (1996) High resolution intravascular MRI and MRS by using a catheter receiver coil. *Magnetic Resonance in Medicine*, 36(4), 596-605.
15. Crottet, D., Menli, R., Wicky, S. and van der Kink, J.J. (2002) Reciprocity and sensitivity of opposed-solenoid endovascular MRI probes. *Journal of Magnetic Resonance*, 159(2), 219-225.
16. Inui, K., Nakazawa, S., Yoshino, J. et al. (1995) Endoscopic MRI: preliminary results of a new technique for visualization and staging of gastrointestinal tumors. *Endoscopy*, 27(7), 480-485.
17. deSouza, N.M., Coutts, G.A., Larkman, D.J., et al. (2000) Combined MRI and fibreoptic colonoscopy: technical considerations and clinical feasibility. *Minimally Invasive Therapy & Allied Technologies*, 9(1), 25-30.
18. Gilderdale, D.J., Williams, A.D., Dave, U. and deSouza, N.M. (2003) An inductively-coupled, detachable receiver coil system for use with magnetic resonance compatible endoscopes. *Journal of Magnetic Resonance Imaging*, 18(1), 131-135.
19. Burl, M., Coutts, G.A., Herlihy, D. et al. (1999) Twisted-pair RF coil suitable for locating the track of a catheter. *Magnetic Resonance in Medicine*, 41(3), 636-638.
20. Zuehlsdorff, S., Umathum, R., Volz, S. et al. (2004) MR coil design for simultaneous tip tracking and curvature delineation of a catheter. *Magnetic Resonance in Medicine*, 52(1), 214-218.
21. Hillenbrand, C.M., Elhort, D.R., Wong, E.Y. et al. (2004) Active device tracking and high-resolution intravascular MRI using a novel catheter-based opposed solenoid phased array coil. *Magnetic Resonance in Medicine*, 51(4), 668-675.

22. Arepally, A., Georgiades, C., Hofmann, L.V. et al. (2004) Hilar Cholangiocarcinoma: staging with intrabiliary MRI. *American Journal of Roentgenology*, 183(4), 1071-1074.
23. Kozarek, R. (2007) Biliary ERCP. *Endoscopy*, 39(1), 11-16.
24. Quick, H.H., Ladd, M.E., Zimmermann-Paul, G.G., et al. (1999) Single-loop coil concepts for intravascular magnetic resonance imaging. *Magnetic Resonance in Medicine*, 41(4), 751-758.
25. Atalar. E. (2012) Catheter coils. pp. 211-223 in *RF coils for MRI*, Vaughan, J.T. and Griffiths, J.R., Eds., John Wiley and Sons, Chichester.
26. Sathyanarayana, S. and Bottomley, P.A. (2009) MRI endoscopy using intrinsically localized probes. *Medical Physics*, 36(3), 908-919.
27. Ocali, O. and Atalar, E. (1997) Intravascular magnetic resonance imaging using a loopless catheter antenna. *Magnetic Resonance in Medicine*, 37(1), 112-118.
28. Susil, R.C., Yeung, C.J. and Atalar, E. (2003) Intravascular extended sensitivity (IVES) MRI antennas. *Magnetic Resonance in Medicine*, 50(2), 383-390.
29. Qian, D., El-Sharkawy, A.M., Atalar, E. and Bottomley, P.A. (2010) Interventional MRI: tapering improves the distal sensitivity of the loopless antenna. *Magnetic Resonance in Medicine*, 63(3), 797-802.
30. Hoult, D.I. and Richards, R.E. (1976) The signal-to-noise ratio of the nuclear magnetic resonance experiment. *Journal of Magnetic Resonance*, 24(1), 71-85.
31. Schnall, M.D., Barlow, C., Subramanian, V.H. and Leigh, J.S. (1986) Wireless implanted magnetic resonance probes for *in vivo* NMR. *Journal of Magnetic Resonance*, 68(1), 161-167.
32. Hyde, J.S., Rilling, R.S. and Jesmanowicz, A. (1990) Passive decoupling of surface coils by pole insertion. *Journal of Magnetic Resonance*, 89(3), 485-495.
33. Edelstein, W.A., Hardy, C.J. and Mueller, O.M. (1986) Electronic decoupling of surface coil receivers for NMR imaging and spectroscopy. *Journal of Magnetic Resonance*, 67(1), 156-161.
34. Goubau, G. (1950) Surface waves and their application to transmission lines. *Journal of Applied Physics*, 21(11), 1119-1128.

35. Acikel, V. and Atalar E. (2011) Modelling of radiofrequency currents on lead wires during MR imaging using a modified transmission line method. *Medical Physics*, 38(12), 6623-6632.
36. Surowiec, A., Stuchly, S.S., Eidus, L. and Swarup, A. (1987) In-vitro dielectric properties of human tissue at radio frequencies. *Physics in Medicine and Biology*, 32(5), 615-621.
37. Konings, M.K., Bartels, L.W., Smits, H.F.M. and Bakker, C.J.G. (2000) Heating around intravascular guidewires by resonating RF waves. *Journal of Magnetic Resonance Imaging*, 12(1), 79-95.
38. Nitz, W.R., Oppelt ,A., Renz ,W. et al. (2001) On the heating of linear conductive structures as guidewires and catheters in interventional MRI. *Journal of Magnetic Resonance Imaging*, 13(1), 105-114.
39. Atalar, E. (1999) Safe coaxial cables" *Proceedings of the 7th Annual Meeting of ISMRM*, Philadelphia, PA, May 24-28, p. 1006.
40. Ladd, M.E. and Quick H.H. (2000) Reduction of resonant RF heating in intravascular catheters using coaxial chokes. *Magnetic Resonance in Medicine*, 43(4), 615-619.
41. Bottomley, P.A., Kumar, A., Edelstein, W.A. et al. (2010) Designing passive MRI-safe implantable conducting leads with electrodes. *Medical Physics*, 37(7), 3828-3843.
42. Weiss, S., Vernickel, P., Schaeffter, T. et al. (2005) Transmission line for improved RF safety of interventional devices. *Magnetic Resonance in Medicine*, 54(1), 182-189.
43. Krafft, A., Müller, S., Umathum, R. et al. (2006) B_1 field-insensitive transformers for RF-safe transmission lines. *Magnetic Resonance Materials in Physics*, 19(5), 257-266.
44. Shamonina, E., Kalinin, V.A., Ringhofer, K.H and Solymar, L. (2002) Magnetoinductive waveguide. *Electronics Letters*, 38(8), 371-373.
45. Wiltshire, M.C.K., Shamonina, E., Young, I.R. and Solymar, L. (2003) Dispersion characteristics of magneto-inductive waves: comparison between theory and experiment. *Electronics Letters*, 39(2), 215-217.
46. Webb, A.G. (2012) Microcoils", pp. 224-232 in *RF coils for MRI*, Vaughan, J.T. and Griffiths, J.R., Eds., John Wiley and Sons, Chichester.
47. Peck, T.L., Magin, R.L., Kruse, J., Feng, M. (1994) NMR microspectroscopy on 100-μm planar RF coils fabricated on gallium arsenide substrates, *IEEE Transactions on Biomedical Engineering*, 41(7), 706-709.

48. Massin, C., Boero. C., Vincent, F. et al. (2002) High-Q factor RF planar microcoils for micro-scale NMR spectroscopy. *Sensors and Actuators A*, 97-8, 280-288.
49. Coutrot, A.-L., Dufour-Gergam, E., Quemper, J.-M. et aL. (2002) Copper micromolding process for NMR microinductors realisation. *Sensors and Actuators A*, 99(1-2), 49-54.
50. Uelzen, Th., Fandrey, S., Müller, J. (2006) Mechanical and electrical properties of electroplated copper for MR-imaging coils. *Microsystems Technology*, 12(4), 343-351.
51. Woytasik, M., Ginefri, J.-C., Raynaud, J.-S. et al. (2007) Characterisation of flexible RF microcoils dedicated to local MRI. *Microsystems Technology*, 13(11), 1575-1580.
52. Ellersiek, D., Fassbender, H., Bruners, P. et al. (2010) A monolithically fabricated flexible resonant circuit for catheter tracking in magnetic resonance imaging. *Sensors and Actuators B*, 144(2), 432-436.
53. Rogers, J.A., Jackman, R.J., Whitesides, G.M. et al. (1997) Using microcontact printing to fabricate microcoils on capillaries for high resolution proton nuclear magnetic resonance on nanoliter volumes. *Applied Physics Letters*, 70(18), 2464-2466.
54. Malba, V., Maxwell, R., Evans, L.B. et al. (2003) Laser-lathe lithography – a novel method for manufacturing nuclear magnetic resonance microcoils. *Biomedical Microdevices*, 5(1), 21-27.
55. Badilita V., Kratt K., Baxan N. et al. (2010) On-chip three dimensional microcoils for MRI at the microscale. *Lab Chip*, 10, 1387-1390.
56. Ahmad, M.M., Syms, R.R.A., Young, I.R. et al. (2009) Catheter-based flexible microcoil RF detectors for internal magnetic resonance imaging. *Journal of Micromechanics and Microengineering*, 19(7), 074011.
57. Grieg, D.D. and Engelmann, H.F. (1952) Microstrip - a new transmission technique for the kilomegacycle range. *Proceedings of the Institute of Radio Engineers*, 40(12), 1644-1650.
58. Wen, C.P. (1969) Coplanar waveguide: a surface strip transmission line suitable for nonreciprocal gyromagnetic device applications. *IEEE Transactions on Microwave Theory and Techniques*, 17(12), 1087-1990.
59. Kahrizi, M., Sarkar, T.K. and Maricevic Z.A. (1994) Dynamic analysis of a microstrip line over a perforated ground plane. *IEEE Transactions on Microwave Theory and Techechniques*, 42(5), 820-825.

60. Syms, R.R.A., Segkhoonthod, K. and Young I.R. (2011) Periodically structured thin-film cables. *Institution of Engineering and Technology Proceedings on Microwaves, Antennas and Propagation*, 5(9), 1123-1129.
61. Syms, R.R.A., Young, I.R., Ahmad, M.M. et al. (2010) Thin-film detector system for internal magnetic resonance imaging. *Sensors and Actuators A*, 163(1), 15-24.
62. Syms, R.R.A., Solymar, L. and Young, I.R. (2010) Periodic analysis of MR-safe transmission lines. *IEEE Journal on Selected Topics in Quantum Electronics*, 16(2), 433-440.
63. Syms, R.R.A., Young, I.R., Solymar, L. and Floume, T. (201) Thin-film magneto-inductive cables. *Journal of Physics D: Applied Physics*, 43(5), 055102.
64. Syms, R.R.A. and Solymar, L. (2010) Bends in magneto-inductive waveguides. *Metamaterials*, 4(4), 161-169.
65. Wiltshire, M.C.K. and Syms, R.R.A. (2014) Noise performance of magnetoinductive cables. *Journal of Applied Physics*, 116(3), 034503.
66. Syms, R.R.A., Young, I.R., Ahmad, M.M. and Rea M. (2012) Magnetic resonance imaging with linear magneto-inductive waveguides. *Journal of Applied Physics*, 112(11), 114911.
67. Segkhoonthod, K., Syms, R.R.A., Young, I.R. (2014) Design of magneto-inductive magnetic resonance imaging catheters. *IEEE Sensors Journal*, 14(5), 1505-1513.
68. Syms, R.R.A., Young I.R. and Rea M. (2013) Frequency scaling of catheter-based magneto-inductive MR imaging detectors. *Proceedings of the 17th Transducers Conference*, Barcelona, Spain, June 16-20, 594-597.
69. Dupont (2006) Kapton® HN Polyimide Film Data Sheet K-15345.
70. Kardoulaki, E., Syms R.R.A., Young, I.R. et al. (2015) Thin-film microcoil detectors: application in MR-thermometry. *Sensors and Actuators A*, 226, 48-58.
71. Kardoulaki, E., Syms, R.R.A., Young, I.R. et al. (2015) Opto-thermal profile of an ablation catheter with integrated micro-coil for MR-thermometry during Nd: YAG laser interstitial thermal therapies of the liver – an in-vitro experimental and theoretical study. *Medical Physics*, 42(3), 1389-1397.
72. Syms, R.R.A., Young, I.R., Ahmad, M.M. et al. (2013) Magneto-inductive catheter receiver for magnetic resonance imaging. *IEEE Transactions on Biomedical Engineering*, 60(9), 2421-2431.

73. Kramer, H.W. (2001) Microbore catheters: keys to successful design and manufacture, Part I. *Medical Device Technology*, October Issue, 14-16.
74. Syms, R.R.A., Young, I.R., Wadsworth, C.A. et al. (2013) Magnetic resonance imaging duodenoscope. *IEEE Transactions on Biomedical Engineering*, 60(12), 3458-3467.
75. Kardoulaki, E., Syms, R.R.A., Young, I.R. and Rea M. (2016) SNR in MI catheter receivers for MRI" *IEEE Sensors Journal*, to be published

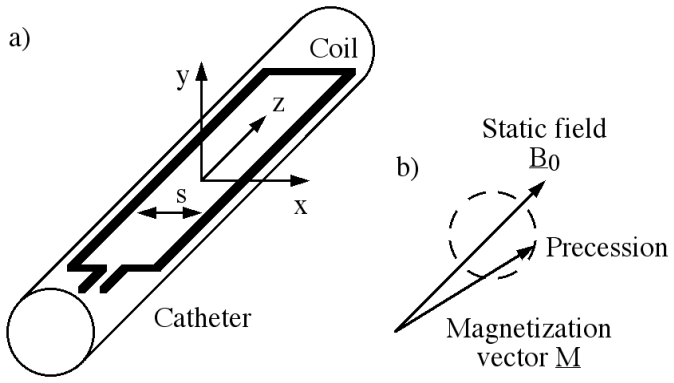

Figure 1. MRI signal reception: a) elongated loop catheter coil and b) precessing magnetization vector.

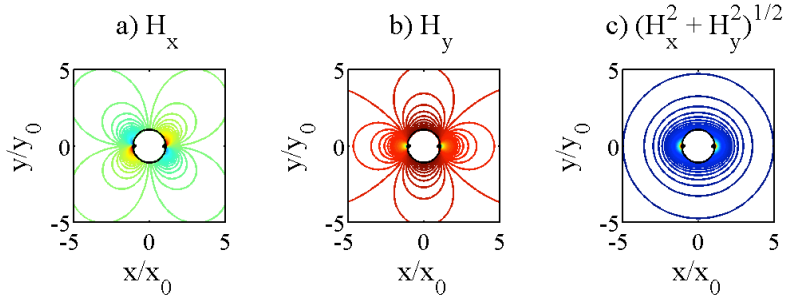

Figure 2. Detection sensitivity patterns for a two-wire coil: a) H_x, b) H_y and c) $\sqrt{(H_x^2 + H_y^2)}$.

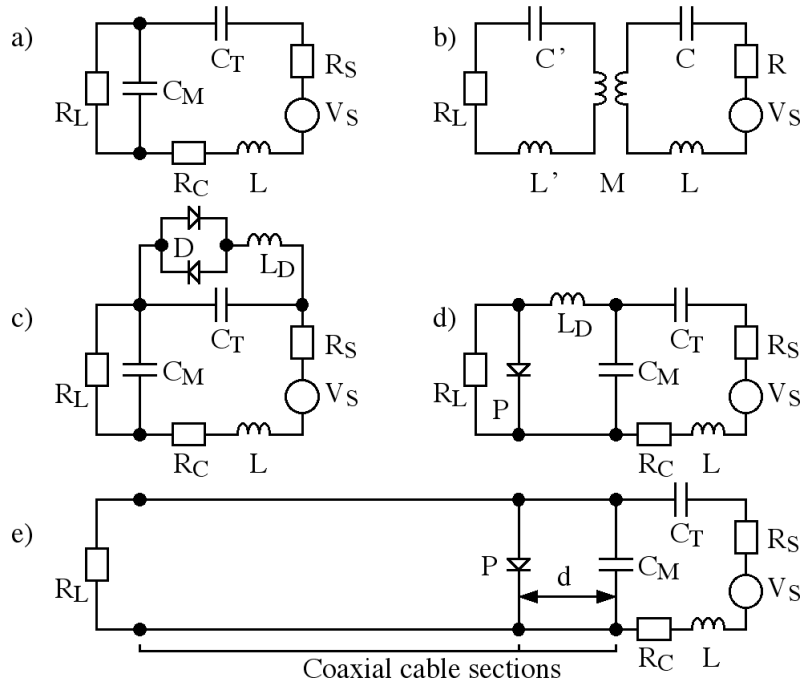

Figure 3. Equivalent circuits of resonant detectors: a) and b) series capacitor and mutual inductance matching, c) and d) passive and active decoupling, and e) coaxial output.

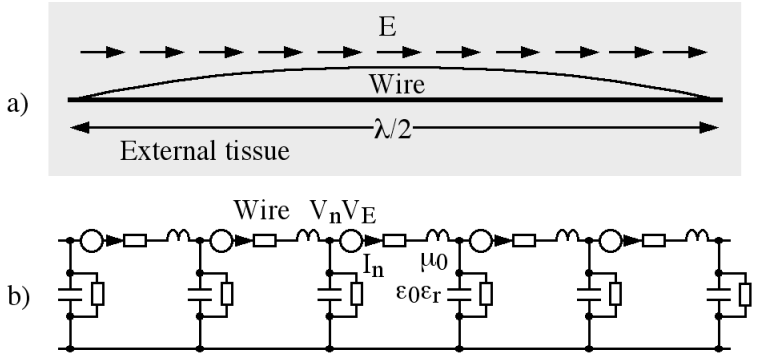

Figure 4. Excitation of standing surface waves on an immersed linear conductor by an electric field: a) physical arrangement, and b) equivalent circuit model.

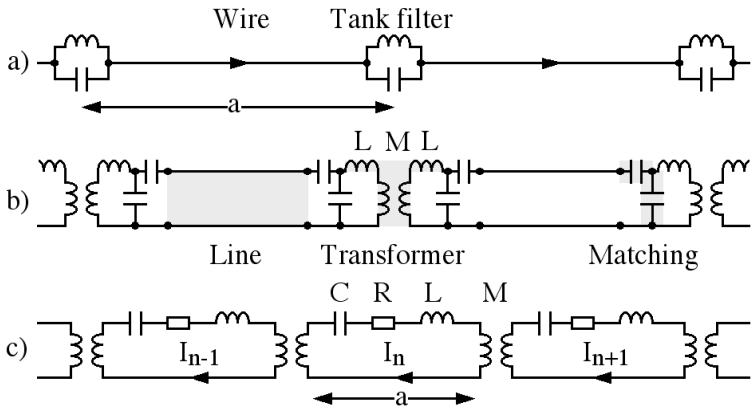

Figure 5. Prevention of surface wave resonances: a) insertion of current-blocking impedances, b) transformer segmentation, and c) use of magneto-inductive waveguides. © 2010 IEEE. Reprinted, with permission, from [62].

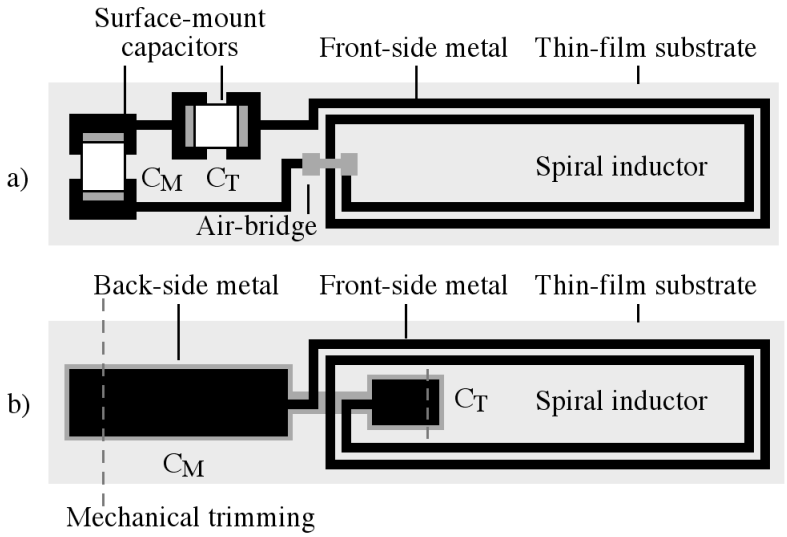

Figure 6. Planar spiral inductors, with a) hybrid and b) integrated capacitors.

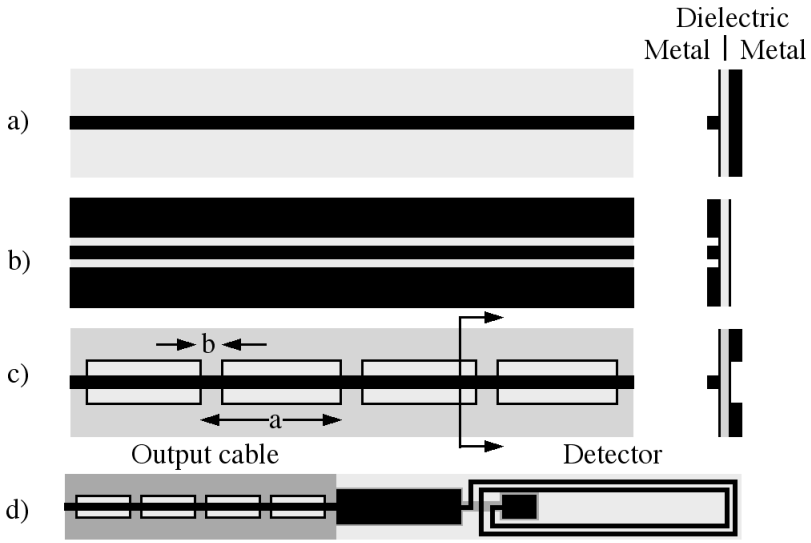

Figure 7. Planar interconnects: a) microstrip, b) coplanar waveguide, c) electromagnetic bandgap waveguide; d) complete receiver combining resonant detector with EBG output cable. Reprinted from [61] , Copyright 2010, with permission from Elsevier.

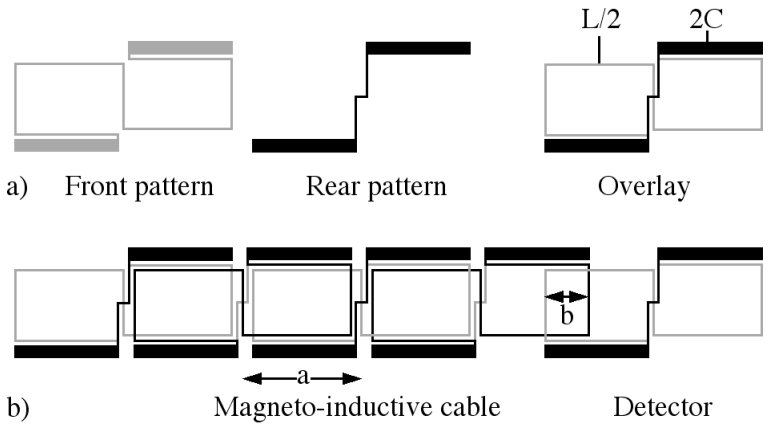

Figure 8. Magneto-inductive receivers: a) single figure-of-eight element and b) complete receiver combining resonant detector with MI output cable. Reprinted with permission from [66]. Copyright 2012, AIP Publishing LLC.

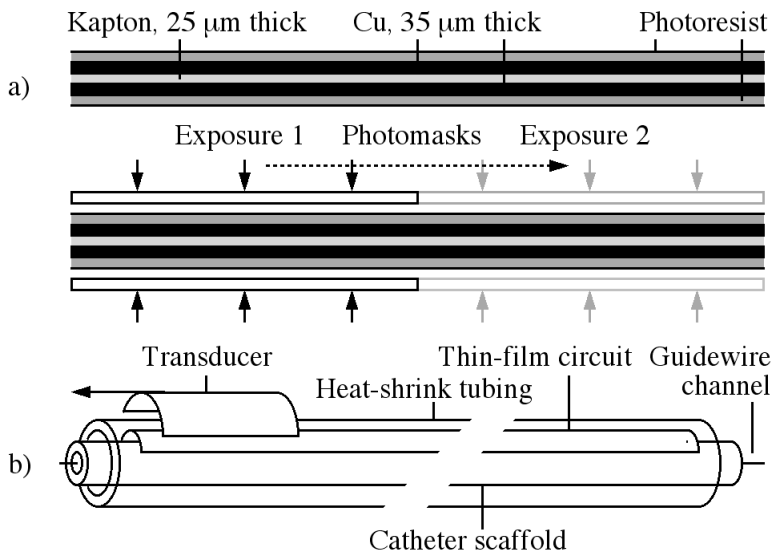

Figure 9. a) Double-sided patterning for thin-film circuit fabrication, and b) catheter construction. Reprinted from [61], Copyright 2010, with permission from Elsevier.

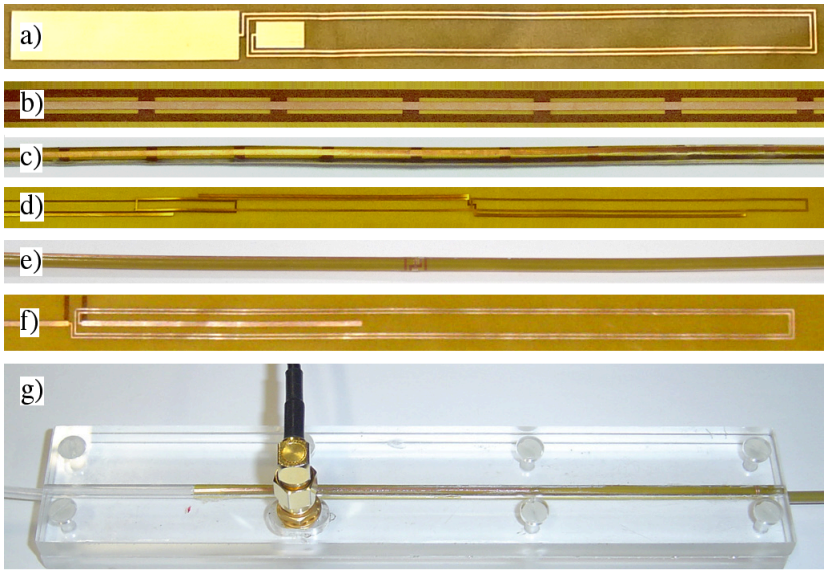

Figure 10. Completed thin film circuits: a) spiral microcoil, b) and c) EBG waveguide unmounted and mounted on catheter; d) and e) MI waveguide unmounted and mounted on catheter; f) and g) resonant transducer, flat and attached to MI catheter.

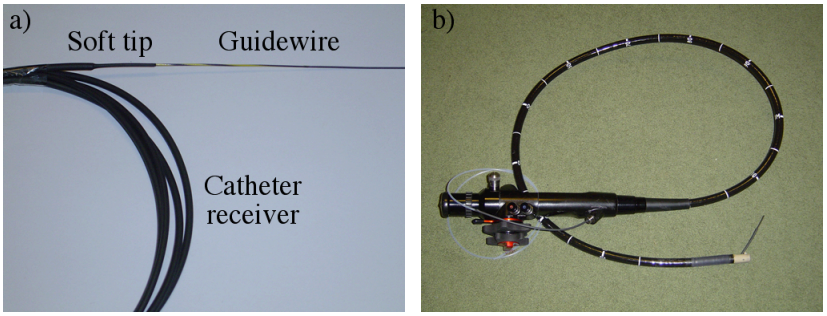

Figure 11. Magneto-inductive catheter receiver: a) mounted on guidewire, and b) passing through biopsy channel of non-magnetic duodenoscope.

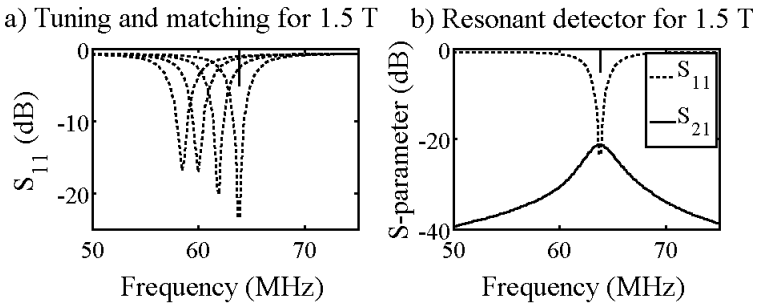

Figure 12. Frequency variation of scattering parameters for resonant spiral microcoil, a) during and b) after tuning and matching for operation at 1.5 T.

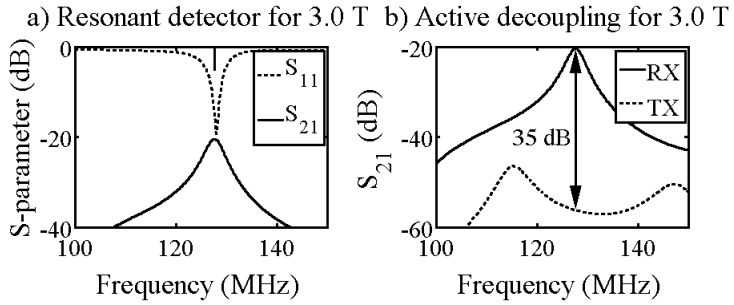

Figure 13. Frequency variation of scattering parameters for resonant spiral microcoil, a) after tuning and matching for operation at 3.0 T and b) during active decoupling.

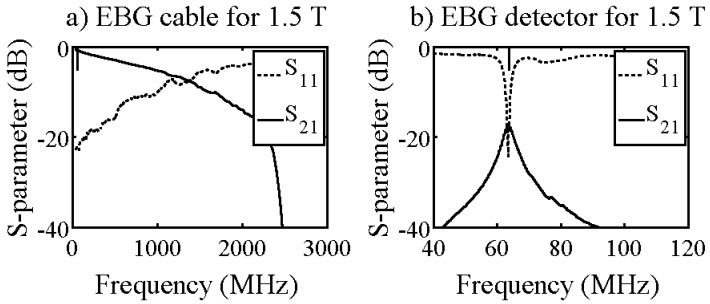

Figure 14. Frequency variation of scattering parameters for a) two-metre long EBG waveguide and b) EBG receiver tuned for operation at 1.5 T.

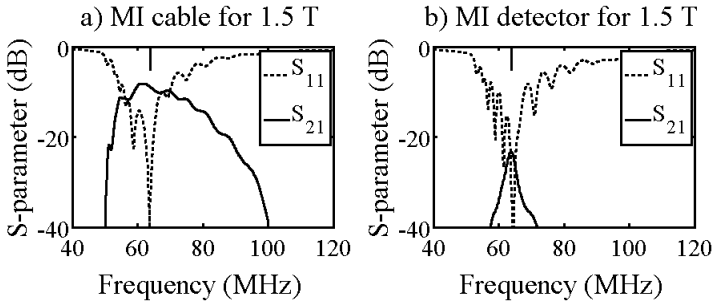

Figure 15. Frequency variation of scattering parameters for a) two metre long MI waveguide and b) MI receiver tuned for operation at 1.5 T. © 2013 IEEE. Reprinted, with permission, from [72].

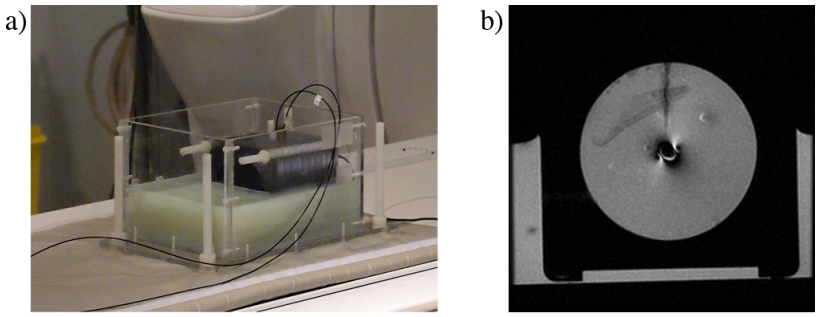

Figure 16. Microcoil evaluation at 3.0 T: a) phantom imaging experiment, and b) axial array coil image showing cylindrical gel phantom with microcoil at centre.

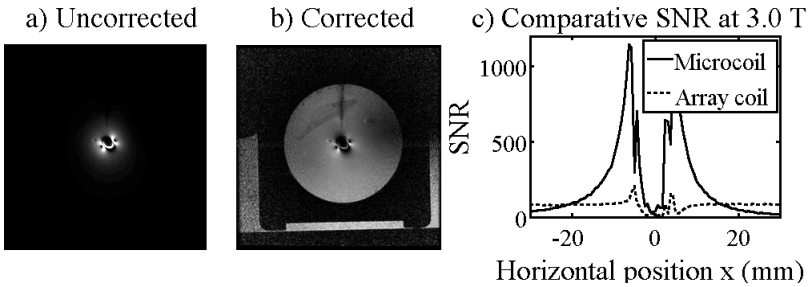

Figure 17. Microcoil evaluation at 3.0 T: a) and b) axial images of gel phantom obtained using microcoil, before and after correction for radial sensitivity variation, and c) comparative variations of SNR for microcoil and array coil.

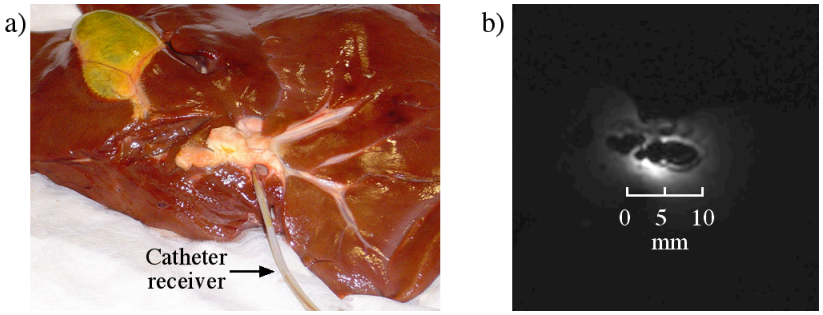

Figure 18. EBG catheter receiver evaluation at 1.5 T: a) catheter receiver inside in vitro liver specimen, and b) uncorrected axial slice image of duct al system.

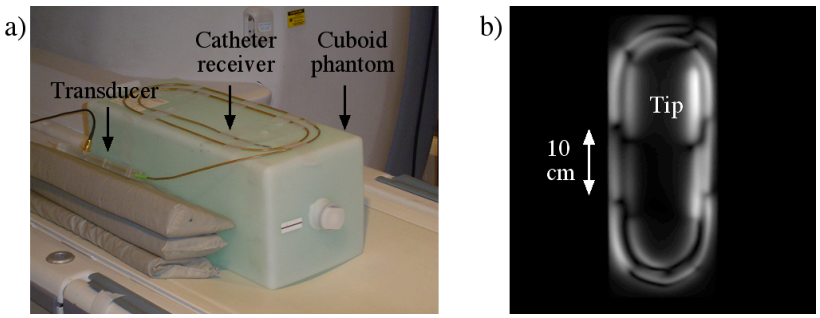

Figure 19. MI catheter receiver evaluation at 1.5 T: a) phantom specimen with catheter spiralled on cuboid, and b) coronal slice image beneath catheter. Reprinted with permission from [66]. Copyright 2012, AIP Publishing LLC.

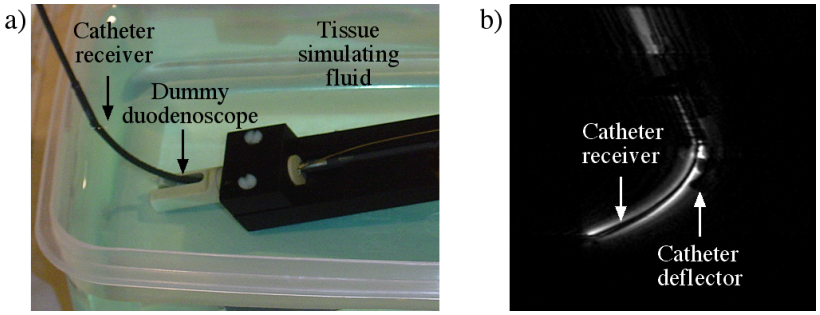

Figure 20. MI catheter receiver evaluation at 1.5 T: a) phantom specimen with catheter in dummy duodenoscope tip, and b) sagittal slice image through catheter. © 2013 IEEE. Reprinted, with permission, from [72].